Virtual-Real Interaction And Status Monitoring Of WK35 Bucket Long-Distance Laser Heating System Based On Digital Twin

Jiayue Yu[1*], Xiaowen Song[1], He Lv[1], and Bin Yu[2]

[1] *Virtual-Real Interaction and Status Monitoring of WK35 Bucket Long-Distance Laser Heating System Based on Digital Twin*
[2] *Xilinhot Chenda Human Resources Service Co., Ltd. Xilinhot, 026000, China*
[*] *Corresponding author. E-mail: 15547156928@163.com*

Received: July 15, 2026; Accepted: August 17, 2026

Remote laser heating of WK35 buckets faces several constraints, including late-state detection, empirical parameter settings, and inadequate synchronization between the physical and virtual spaces, which affect the quality and stability of the heating process. This research aims to develop a monitoring and control system for the heating process by applying the digital twin concept, including multi-source sensing, two-way physical and virtual interaction, and intelligent prediction. The first stage includes the sensing of temperature, laser power, and movement trajectories and their synchronization with the dynamic virtual model. Meanwhile, the second stage includes the return of the results of digital twin operations to the physical world and adaptive adjustment of heating parameters depending on the current state. The states of the equipment and faults are detected with the help of closed-loop control and Transformer-BiLSTM spatiotemporal feature fusion algorithms. As a result of the experimental study, it was found that the reduction of synchronization error in comparison with the classical PID control system, no power overshoots were detected below 0.05 kW, and stabilization was reached within 0.8 seconds. The temperature of the main heating area was rather constant and equal to 965°C and the AUC of the anomaly detection algorithm was 0.96.

Keywords: Digital twin technology; Virtual–physical interaction; Laser heating system; State monitoring and prediction; Transformer-BiLSTM model

© The Author('s). This is an open-access article distributed under the terms of the Creative Commons Attribution License (CC BY 4.0), which permits unrestricted use, distribution, and reproduction in any medium, provided the original author and source are cited.

http://dx.doi.org/10.6180/jase.202612_35.051

1. Introduction

The long-distance laser heating technique is important in maintaining the durability of WK35 mining buckets under harsh operating conditions in terms of extreme wear and shock loading due to its impact on the lifespan and safety of the machine [1, 2]. The process shows complex temperature distributions and varying power dynamics [3, 4]. However, traditional manual control cannot provide an appropriate response to sudden variations in the laser power, temperature, and machinery status [5, 6]. Existing control systems based on discrete sensors give inaccurate control, overheating in a local region, and delayed detection of anomalies [7, 8].

Infrared thermal imaging can be used in temperature measurement, but it does not provide efficient feedback. For example, Feng et al. [9] do not use multisource fusion and real-time synchronization. Gaikwad et al. [10] miss bidirectional virtual physical control, Di Meglio et al. [11] disregard synchronization of curvilinear or irregular structures, and Aminzadeh et al. [12] cannot provide asynchronous multisensor sampling and anomaly early warning. Finite-element method and sensor-based techniques similarly limit the possibilities for virtual physical synchronization and interaction [13, 14]. Methods of temperature prediction-based control and optimization are faced with similar restrictions [15–18].

Digital modeling, virtual simulation, and intelligent prediction have enhanced monitoring techniques for long-distance laser heating [19, 20], but low update frequencies prevent real-time anomaly detection [21, 22]. IoT and time series techniques are limited in terms of multisource fusion [23, 24]. Besides, deep learning and finite-element methods cannot provide intelligent interaction [25, 26]. Therefore, problems with multisource fusion, virtual physical synchronization, and intelligent assessment of machinery status still exist [27, 28].

The literature review on this topic is divided into three different categories with the aim of emphasizing some of the research issues associated with this topic. It has been observed that existing multi-source sensor technologies work independently while gathering data, which leads to data isolation and delay in the estimation of states. The interaction process, both virtual and physical, is unidirectional, where no feedback is given from the virtual model to the physical environment for optimization of parameters. Also, traditional time series models are incapable of capturing the dependencies between various variables such as the temperature field and power changes.

This work designs a digital twin system for remote laser heating of WK35 buckets in order to solve problems related to the experience-based tuning of parameters, late recognition of the state of equipment, and the synchronization of virtual and physical objects. The temperature, laser power, and motion data are collected by multiple sensors to construct a dynamic digital twin in real time that maps between the physical and the virtual world.

2. Methods

2.1. Construction of Multi-Source Sensing Network for WK35 Bucket Laser Heating

The IR thermometer, laser power detector, current detector, and displacement detector are used to ensure the observability of the entire system state while remotely heating the WK35 bucket with laser light. These sensors detect the surface temperature, changes in the laser power, operating current, scan path, and accuracy of actuator motion [29, 30]. Zero-point and range calibration are carried out for all sensors using a black body source and displacement stage.

In the process of collecting data, synchronization is achieved through the use of a master-clock-based scheme for the synchronization of timestamps at all the sensors. The multiple-source system observation vector at time t is defined as:

$$X(t) = [T_1(t), T_2(t), \ldots, T_n(t), P(t), I(t), D(t)] \quad (1)$$

Here, $T_n(t)$, $P(t)$, $I(t)$, and $D(t)$ represent temperature, laser power, current, and actuator displacement, respectively. Kalman filtering iteratively removes any noise and disturbance present. The state update equation is:

$$\hat{x}_k = \hat{x}_{k-1} + K_k(z_k - H\hat{x}_{k-1}) \quad (2)$$

z_k is the current observation value; H is the observation matrix; and K_k is the Kalman gain, used to dynamically correct measurement errors, thereby improving the stability and consistency of multi-source data.

The communication-based viewpoint sees the standardization of heterogeneous sensor data by the industrial data bus standard based on OPC UA. The sensor data are captured in real time at the edge computing nodes, transformed to the unified form, and pre-processed by filtering out the outliers, applying sliding window smoothing, and normalizing in order to avoid the effect of communication delay.

In order to create the digital twin model, the multi-source features of different dimensions need to be further standardized in the same feature space. The following is the expression of normalized features:

$$x_i'(t) = \frac{x_i(t) - \mu_i}{\sigma_i} \quad (3)$$

Here, $x_i(t)$ represents the starting value, whereas μ_i and σ_i are the mean and standard deviation, respectively. The standardization of temperature, power, current, and displacement ensures that the information can be represented in one common feature space, and this indicates that the scale variance will not have any effect on the model in use. Consequently, the multisensor network offers real-time access to the information stream from the multisensor network to the digital twin layer using edge-cloud collaboration.

2.2. Digital Twin Dynamic Mapping Model for Heating Process

This high-density multi-view point cloud data can be obtained through the 3D laser scanning of the WK35 bucket. Registration and stitching of the point clouds give rise to the formation of the complete geometry model, which is then subjected to processes of denoising, hole filling, and smoothing. The mesh model is obtained from the process of Poisson Reconstruction (Fig. 1). The final stage in the modeling process involves scaling of the model and orienting its coordinate system according to the installed WK35 bucket.

Upon completion of the geometric reconstruction, the 3D model is exported to Unity3D, whereby the heated zone, bucket structure, and motion parts are modeled separately

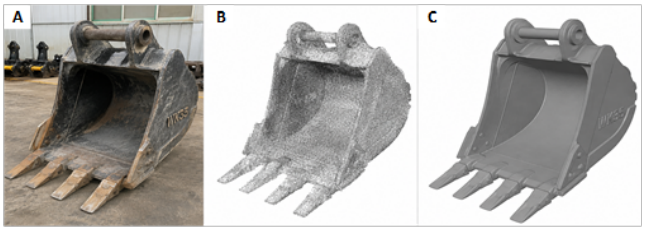


Fig. 1. WK35 Bucket Entity, 3D Point Cloud Model, and Triangular Mesh Model

as physical bodies. A finite element thermal model is developed for the simulation of heat conduction resulting from the laser operation via solution of the transient heat conduction equation:

$$\rho c \frac{\partial T}{\partial t} = \nabla \cdot (k \nabla T) + Q(x,t) \tag{4}$$

In this case, ρ denotes material density, k is thermal conductivity, T denotes temperature field, and $Q(x,t)$ represents the laser heat source. Meshing helps determine dynamic temperature.

FE analysis uses tetrahedral elements with a maximum element size of 3 mm within the heating region and 8 mm elsewhere (total of 187,432 elements). The time-step size of the simulation is $\Delta t = 0.05$ s (0-10 s), 0.10 s (10-100 s) and 0.02 s for cooling. The boundary condition is convective for exposed surfaces with $h = 15\ \mathrm{W/m^2 \cdot K}$, $T_\infty = 20°\mathrm{C}$, while the bottom surface is thermally insulated. The laser heat source is defined by a Gaussian heat flux with $r = 8$ mm and $\eta = 0.45$.

For Dynamic Synchronization, temperature, power, and displacement are saved from the time-aligned vectors on the edge server to update the twin model. In case of deviation in the physical state vector beyond a certain value, only the affected FE model will be updated for computation efficiency and synchronization accuracy. If $(S_p(t))$ and $(S_v(t))$ are physical and virtual state vectors, the synchronization error is defined as:

$$E(t) = |S_p(t) - S_v(t)|_2 \tag{5}$$

The correction procedure for the model starts at the moment when the synchronization error $E(t)$ exceeds a certain value. In this way, one can make some correction of material characteristics and boundary conditions to achieve better convergence. However, the choice of the threshold is a trade-off between accuracy and computational costs: $E_{th} = 1.0°\mathrm{C}$ provides a mean error equal to 0.8°C, 8.2 recalculations per second and 46.3% of resource usage while $E_{th} = 5.0°\mathrm{C}$ leads to a mean error equal to ∼4.3°C and 3.6 recalculations per second but only 8.1% of CPU usage. Hence, the threshold value equals $E_{th} = 2.5°\mathrm{C}$, providing a mean error of 1.2°C, 3.6 recalculations per second, and 19.7% of resource usage.

The coordinates of the displacement sensor as well as the motion controller are described in three-dimensional orientation using quaternions to avoid singularities. The calculated orientation is synchronized in real-time with the Unity rigid body with millisecond precision [31, 32].

Geometry and thermal modeling and synchronization allow the construction of the digital twin for the bucket motion.

2.3. Intelligent Interaction Mechanism for Laser Heating with Virtual-Real Fusion

The communication link between the physical and the digital twin is an MQTT bus. The MQTT broker at the edge provides live streaming of temperature, energy, current, and displacement through JSON messages via topics for homogeneous communication [33, 34].

In the other direction, the digital twin performs consistency analysis and anomaly detection based on live temperatures and the state of the devices. The temperature gradient is being tracked using the sliding window of temperatures across spatial locations:

$$\nabla T_i(t) = T_i(t) - \frac{1}{n} \sum_{j=1}^{n} T_j(t) \tag{6}$$

$T_i(t)$ stands for the temperature measurement at i-th sensor point, and n denotes the number of neighboring sensors in total. Such a method helps detect any anomalies related to overheating or underheating along with the temperature profile in the past.

If the anomaly takes place, the virtual model generates optimal control strategies according to the rules controlling laser power, path, and heating zone. The result will be presented in the form of vectors:

$$u(t) = [P(t), v(t), \theta(t)] \tag{7}$$

Here, $P(t)$ denotes laser power adjustment, $v(t)$ the scanning speed, and $\theta(t)$ the trajectory deflection angle. A constrained optimization model limits the control vector within equipment and safety boundaries to ensure stable operation.

Control commands are transmitted from the digital twin to the laser-controller PLC via the MQTT downlink, converted into low-level signals for power modulation and trajectory replanning, and verified through execution feedback.

The total time delay of the loop consists of the virtual-real interaction $T_{\text{loop}} = T_{\text{uplink}} + T_{\text{edge}} + T_{\text{downlink}} + T_{\text{plc}}$.

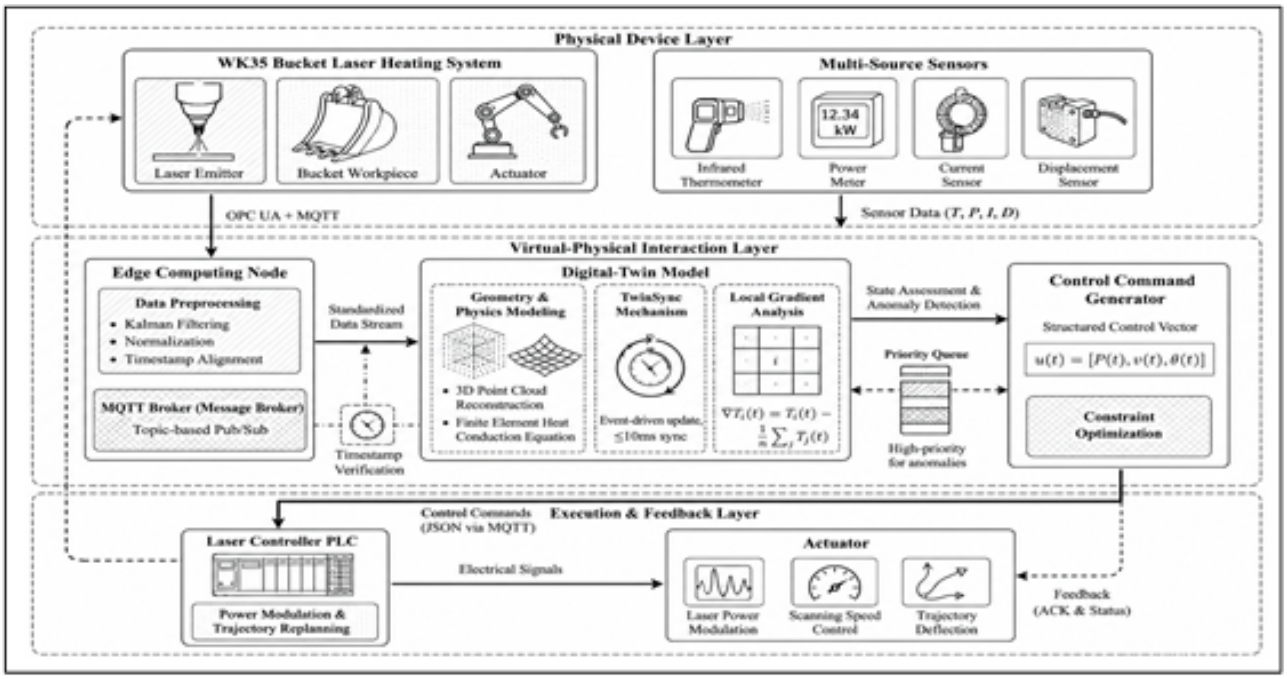


Fig. 2. Overall Framework of the Virtual-Real Fusion Laser Heating Intelligent Interaction Mechanism

In the case of the proposed architecture, T_{uplink} averages 2.5 ms, and T_{edge} includes preprocessing (1.2 ms), finite element calculations (4.5 ms), and 3D visualization (2.1 ms), which gives 7.8 ms. T_{downlink} averages and T_{plc} averages are 3.2 and 5.6 ms, respectively, and therefore the total time delay is 20.0 ms and satisfies the requirement.

With an aim to minimize the effect of latency in the network, priority queuing is employed in the message bus for the abnormal condition messages, and so the temperature deviation and equipment deviation can first take part in the cycle of control and minimize the latency in turn [35, 36]. The timestamp check is the other technique used to ensure synchronization of the uplink/downlink data.

Overall, the interaction mechanism has brought about the cycle of "physical perception-virtual decision making-control feedback" in the digital twin.

The virtual and real fusion of laser heating process has three layers. The physical layer includes the WK35 bucket heating process and consists of the temperature sensor, power sensor, current sensor, and displacement sensor. The collected data from the sensors is transferred through OPC UA and MQTT, with Kalman filtering and normalization. The digital twin layer comprises geometric mapping, finite element analysis for heating, TwinSync, and gradient-based local temperature. The execution layer includes calculating the optimal control vector of laser power, scanning velocity, and trajectory deviation.

Directed communication time delays are $T_{\text{uplink}} = 2.5$ ms, $T_{\text{edge}} = 8.7$ ms, $T_{\text{downlink}} = 3.2$ ms, and $T_{\text{plc}} = 5.6$ ms, respectively. Thus, the total closed-loop time delay will be $T_{\text{loop}} = 20.0$ ms. In conclusion, the proposed architecture allows implementing an intelligent closed-loop architecture for sensing, decision making, and control.

2.4. Equipment Status Monitoring Platform Based on Spatiotemporal Feature Fusion

The Transformer-BiLSTM architecture utilizes a combination of two BiLSTM layers (128 hidden units each way) and a three-layer Transformer encoder (6 attention heads, model dimension 256, FFN 512). Training is done with 0.1 dropout, batch size 64, and 200 epochs with early stopping.

Resampling using sliding windows and filtering using the exponential moving average is performed on the temperature, laser power, and actuator path to ensure synchronization. The hybrid network makes use of spatiotemporal features due to BiLSTM-based temporal dependencies in temperature-power dynamics. State update takes place as Eq. (8):

$$h_t = \text{BiLSTM}(x_t) = [\overrightarrow{h_t}, \overleftarrow{h_t}] \tag{8}$$

x_t represents the multi-source fusion input feature vector at time t, and $\overrightarrow{h_t}$ and $\overleftarrow{h_t}$ display the forward and backward hidden state outputs, respectively. Then, the output sequence of BiLSTM is input into the Transformer encoding module, and the correlation weights between different time steps are modeled through the multi-head self-attention mechanism to realize the enhanced expression of long-term

dependency. The attention calculation Eq. (9):

$$\text{Attention}(Q,K,V) = \text{softmax}\left(\frac{QK^T}{\sqrt{d}}\right)V \tag{9}$$

In this case, Q, K, and V stand for query, key, and value matrices, respectively, with d being the feature dimension scaling. Attention is implemented via the use of temperature, power, and trajectory evolution in combination.

Hyperparameters of Transformer-BiLSTM were determined using an ablation analysis. Sliding window L ranged from 10 to 80, attention heads H: 2, 4, 6, 8, and fully connected layer size N_{fc}: 64, 128, 256, 512. BiLSTM was made of two layers with 128 neurons each. Adam was the optimization algorithm, with LR=1e-3 and decay of 0.9 per 20 epochs. The optimal combination was $L = 40$, $H = 6$, $N_{fc} = 128$ and achieved AUC = 0.95 for anomalies. $L = 20$.

Fig. 3 shows the attention heads of the Transformer model at 20 time intervals. Attention heads 1 and 3 have diagonal weights that denote spatiotemporal dependencies while head 5 denotes long-range dependency and head 7 denotes autoregressive temporal dependency.

For the Health Status Assessment Module, the fused features pass through the regression network and produce the Health Index (HI). It shows the health status of the system when it is in a healthy state. HI is used for health classification and adaptive thresholding. Anomaly occurrence takes place when the decay rate of HI exceeds a certain threshold value. The system's degradation level is obtained using Eq. (10):

$$G(t) = \sqrt{\sum_{i=1}^{N} \omega_i \left(\frac{e_i(t)}{\sigma_i}\right)^2} \tag{10}$$

ω_i represents the feature attention weights adaptively learned by the fully connected network, satisfying $\sum \omega_i = 1$, and N is the dimension of the state variables. Subsequently, $G(t)$ is converted into a health index $HI(t)$ using the Sigmoid normalization mapping function:

$$HI(t) = \frac{1}{1+\exp(\alpha(G(t)-\beta))} \tag{11}$$

Here, α is the parameter of curve sensitivity, and β is the parameter of health baseline shift. The dimensionless $HI(t)$ varies between (0,1), with closeness to 1 indicating a healthy status of the equipment and closeness to 0 indicating degradation/abnormalities.

For prediction and early detection purposes, the status of the equipment in the short term is forecasted through the use of encoded temporal features with the help of a Transformer, and this is compared with the live data using the state residual function:

$$E_t = |\hat{y}_t - y_t|_2 \tag{12}$$

Threshold-crossing residuals prompt multilevel alarms for input into the virtual-real control block for adjusting laser power and speed, completing the control loop. Fusion of multilevel data is used to build a health model for continuous monitoring, fault detection, and forecasting of future states.

Experimental data were gathered using the WK35 bucket laser-heating system at 0-6 kW, 0.1-2.5 m/s, 50 Hz. Public data were transformed into a 3D space of power, temperature, and motion parameters and re-sampled with a frequency of 10 ms. Generated FE data covered the range of 20-80 mm thickness and 35-60 W/mK with power perturbations (+/-30%), offset of laser path (0-15°), and ambient temperature (-10 to +45°C). The last test set consisted of 120 minutes of data with $\sim 4.3\times10^6$ points.

Testing included synchronization error, response time, temperature uniformity, fault detection precision, and power stability in steady state, transition state, and perturbation state (3 repeats for each).

Equipment: Laser (6 kW, wavelength 1070 nm, $M^2 \leq 1.3$); IR temperature sensor, power sensor, IR current sensor, six-axis displacement sensor; Intel Xeon Silver 4314 CPU, RTX 4090 GPU, Gigabit Ethernet, MQTT, Ubuntu 20.04, Unity3D 2022.3, MATLAB/Simulink.

3. Results and discussions

3.1. Evaluation of Virtual-Real Synchronization Delay and Consistency Error

Once the system is operational, temperature, energy, and displacement readings of the physical system and its digital replica will be measured simultaneously, with the edge node used as the clock. End-to-end processing time of the signal from the point of measurement to the moment of update of the virtual system will be measured in order to distinguish uplink latency from the feedback latency. Synchronization accuracy will be determined by the comparison of the state of the physical and the virtual system at the same instant in time, resulting in the generation of an error sequence.

The analysis of synchronization performance from virtual world to real environment is conducted by referring to Fig. 4. From Fig. 4(a), it is seen that the FEA calculation module has the longest time delay value of approximately 4.5 ms, but this time is much shorter compared to other configurations such as no-edge cooperation (12.4 ms) and local computation (8.2 ms). The proposed method is able to reduce the time used in the 3D rendering process to approximately 2.1 ms. From Fig. 4(b), the values of synchronization errors are clustered around 0.6 with a narrow 95% confidence interval range, whereas the peak values of

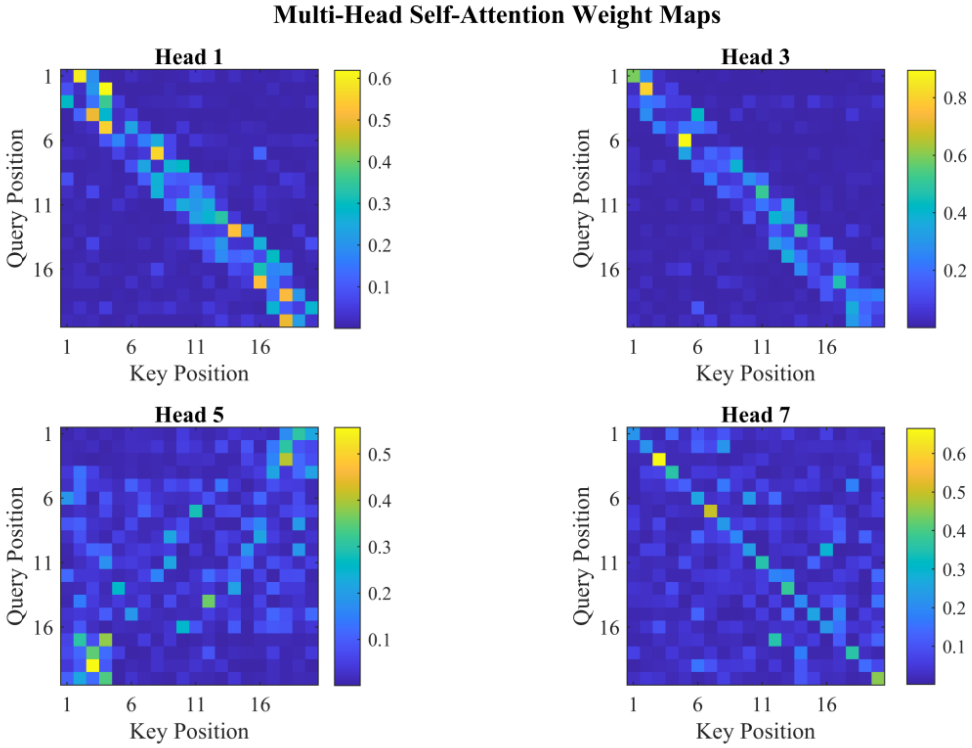


Fig. 3. Multi-Head Self-Attention Weight Heatmap

Table 1. Key Experimental Parameter Configurations

Module	Parameter	Value
Laser	Rated power	6 kW
Laser wavelength	Operating wavelength	1070 nm
Temperature sampling	Frequency	50 Hz
System synchronization period	Time resolution	10 ms
Industrial control platform	GPU	RTX 4090
Communication protocol	Data transmission	MQTT + OPC UA
Temperature range	Test interval	-10°C to 1200°C

average errors for traditional PID control and the LSTM model are 2.4 and 1.5, respectively.

Significance tests were conducted between the proposed model and the baseline models in relation to synchronization efficiency, control performance, and fault detection. The output of the paired-sample t-test showed that the proposed method resulted in significantly lower virtual-real synchronization error than the conventional PID control method ($t = 5.84$), ($p < 0.01$) and improved power regulation response ($p < 0.05$).

3.2. Evaluation of Heating Temperature Uniformity and Spatial Distribution

The position of the fixed points in the heated region of the bucket is continually recorded and plotted in a two-dimensional space to form the temperature field as a function of time. Analysis of the statistical properties of the process of temperature diffusion in different regions is performed to get information on the spatiotemporal heat conduction dynamics and to find overheating or under-heating regions.

The increase in temperature is represented in Fig. 5(a) as follows: 370°C at 3 (20s) to 880°C at 8 (60s) to 955°C at 80s. Fig. 5(b) represents the maximum temperatures: core 965°C, HAZ 390°C, substrate 175°C, and edges approximately 610°C.

The developed technique provides more uniform distribution (8.5°C compared to 15.3°C and 18.1°C) and better performance in terms of anomaly detection (98.5).

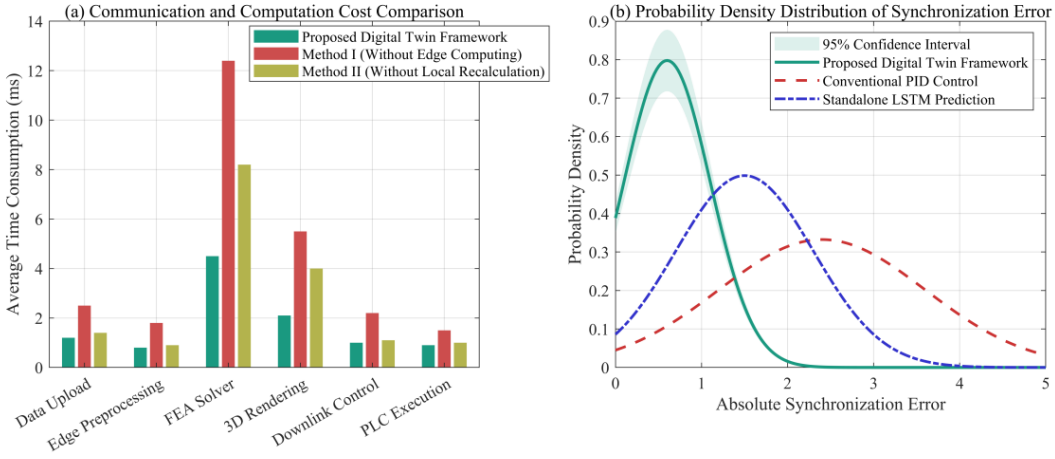


Fig. 4. Evaluation of Virtual-Real Synchronization Delay and Consistency Error, (a) Comparison of Time Consumption of Each Core Communication and Computation Link, (b) Probability Density Distribution of Comprehensive Synchronization Error

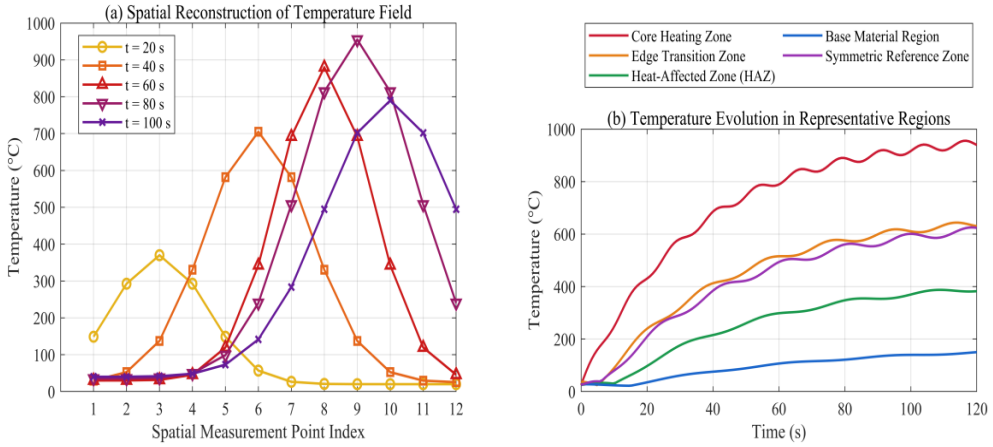


Fig. 5. Evaluation of Heating Temperature Uniformity and Spatial Distribution, (a) Spatial Temperature Distribution, (b) Temperature Evolution Curve of the Region

3.3. Evaluation of Laser Power Control Response Characteristics

For all cases of power tuning, both the command and measured laser power are collected simultaneously until stabilization occurs. Differences in response and settling times are considered along with power-temperature-time behavior.

As depicted in Fig. 6(a), the proposed control technique using twins has a fast response time, with overshoots of 0.04 kW and 0.03 kW, for the ranges 0-3 kW and 3-5 kW, respectively, and reaching steady state within 0.8 seconds. The values are very low when compared with the 0.8 kW overshoot in the case of the conventional PID control technique, thus indicating that the proposed technique is feasible. As can be seen from Fig. 6(b), the average response time of the closed loop for micro amplitude, high frequency disturbance rejection, and continuous step control are 38 ± 1.8 ms, 58 ± 4.2 ms, and 50 ± 3.1 ms, respectively.

3.4. Equipment Status Identification Accuracy and Anomaly Detection Evaluation

The labeling process takes place based on the monitoring tool for the equipment state and is then evaluated against manual or pre-manual inputs in six classes that include: normal, moderate overheating, excessive overheating, yaw scanning, overcurrent, and compound anomalies. Time-series data is partitioned into segments of equal size, which are then labeled and subjected to statistical evaluation. The misclassification process of the samples, peak temperature, and power variations is also analyzed.

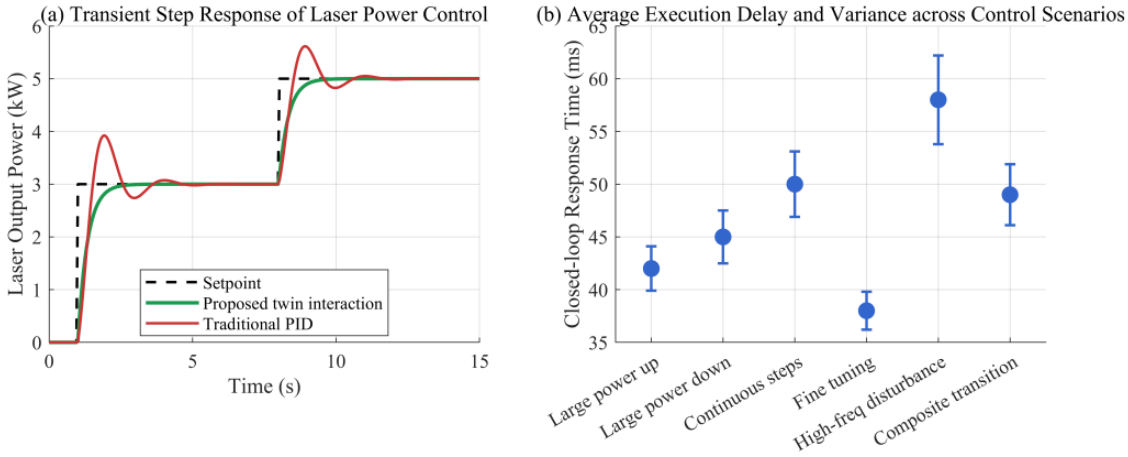


Fig. 6. Evaluation of Laser Power Regulation Response Characteristics, (a) Transient Response Characteristics of Laser Power Sudden Jump Control, (b) Average Execution Delay and Variance Analysis of Commands under Multiple Control Scenarios

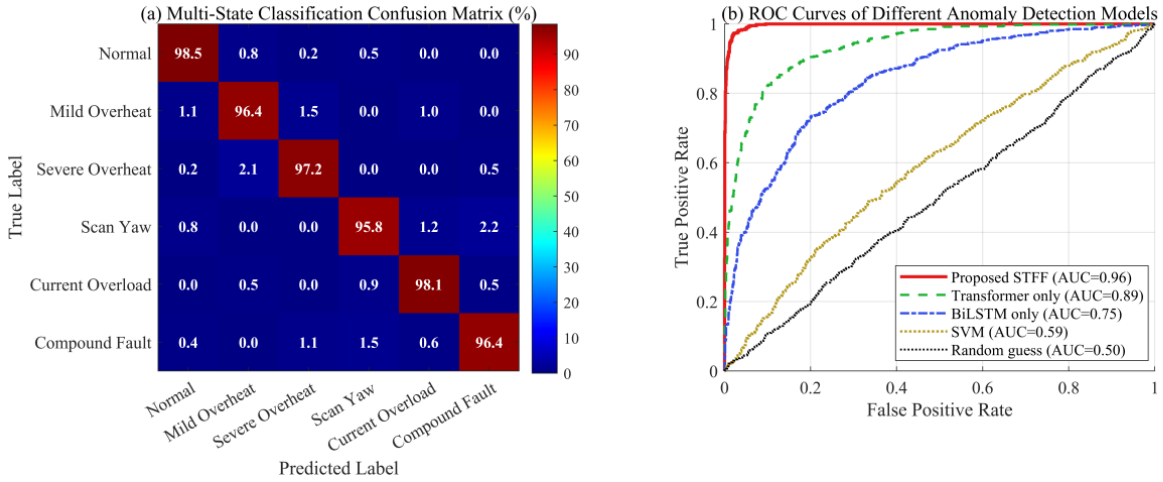


Fig. 7. Equipment Status Identification Accuracy and Anomaly Detection Evaluation, (a) Multi-State Detection Classification Confusion Matrix, (b) Comparison of ROC Curves for Different Anomaly Detection Models

Fig. 7(a) shows that there is high classification performance in six classes, where accuracy of diagonals is more than 95.8%. Accuracy of normal and combined-fault classes is 98.5% and 96.4%, respectively. Major errors include misclassification of mild overheating class into severe overheating class (1.5%), and scan yaw class into combined fault class (2.2%). It is clear from Fig. 7(b) that proposed STFF model achieves AUC of 0.96 and outperforms other models such as Transformer (0.89), BiLSTM (0.75), and SVM (0.59).

3.5. Stability and Operational Fluctuation Assessment of the Heating Process

The important parameters of the heating process, such as temperature changes per unit of time, power changes, and deviations from the optimal actuator position, are permanently measured and separated into equal time segments in order to identify the amount of fluctuations and find any unstable time intervals. The fluctuations at different stages of the process – start, heating, transition, and shutdown – are examined and compared according to their dynamics.

Staging-based variations are provided in Table 2. The first stage is the least stable stage, having a temperature change of 3.52°C/s, power change of 0.28 kW, trajectory change of 0.85 mm, and abnormality rate of 4.2/h. Transition stage I is relatively stable; however, steady heating (20-100 min) is the most stable stage, having a temperature change of 0.12°C/s, power change of 0.04 kW, trajectory change of 0.18 mm, and abnormality rate of 0.40/h. Transi-

Table 2. Statistical Analysis of Fluctuation Intensity and Transition Characteristics of Key Operating Parameters in Different Heating Stages

Heating Stage	Time Window (min)	Mean Temp. Change Rate ± Std (°C/s)	RMS Power Fluctuation (kW)	Max Trajectory Offset (mm)	Abnormal Fluctuation Frequency (times/h)
Start-up phase	0–15	3.52 ± 0.42	0.28	0.85	4.2
Transition I	15–20	1.25 ± 0.18	0.15	0.42	1.5
Steady heating phase	20–100	0.12 ± 0.03	0.04	0.18	0.4
Transition II	100–105	-1.85 ± 0.22	0.12	0.35	0.8
Cooling phase	105–120	-2.45 ± 0.35	0.00	0.05	1.1

tion stage II does not experience much change.

The statistical tests proved a significant difference between the proposed approach, PID, LSTM, and Transformer methods in terms of temperature uniformity ($F(3,76) = 18.34$, $p < 0.001$) and anomaly detection ($F(3,76) = 22.67$, $p < 0.001$). The Tukey HSD test results indicated that the proposed approach significantly excelled other approaches in both cases ($p < 0.01$).

3.6. Ablation Experiment Design and Module Contributions

An ablation study was performed to determine how the individual modules contributed to the performance of the system as a whole. The modules that underwent ablation include the multi-sensing fusion module, the digital twin synchronization module, the MQTT interactive control module, and the prediction module consisting of Transformer-BiLSTM. In order to examine the performance difference between the ablated modules and the entire system, all experiments were conducted under the same heating conditions.

The outcomes of the ablation study are captured in Table 3. The system yields a synchronization error of 1.2°C, temperature uniformity standard deviation of 8.5°C, response delay of 42 ms, and anomaly detection accuracy of 98.5%. Without multi-source sensing fusion, the synchronization error, temperature deviation, and detection accuracy fall to 3.8°C, 18.2°C, and 92.3%, respectively, thereby justifying its significance. The significance of digital twin synchronization can be noted from the fact that its omission results in a synchronization error of 5.6°C, temperature deviation of 22.7°C, and detection accuracy of 88.6%. Though the response delay increases to 76 ms when there is no MQTT control, Transformer-BiLSTM achieves detection accuracy of 86.9%.

It can be said that the significance of digital twin synchronization is higher than that of sensing fusion because of consistency in the physical and virtual states through time and space. Synergy exists between the MQTT and Transformer-BiLSTM modules since timely features are provided by MQTT module for prediction, while important commands are handled through the prediction output. Thus, an ablation result cannot reveal the significance of both modules.

3.7. Performance Evaluation Under Extreme Industrial Conditions

The three extremely harsh environments tested for assessing the generalization performance of the system include: laser power at 6 kW, where the velocity is 2.5 m/s; scanning speed at 3.5 m/s, with laser power of 4 kW; and environmental temperature at -15°C, with laser power at 5 kW. The highest power level caused the synchronization error to rise to 2.8°C from 1.2°C and the power response time to rise to 68 ms because of thermal radiation interference and limitations in the power supply system. In the case of the very high scanning speed, the trajectory error rose to 0.52 mm from 0.18 mm owing to inertia.

4. Conclusions

In this paper, state perception delay, calibration of parameters based on experience, and desynchronization of virtual and physical in WK35 bucket laser heating at a distance through the design of an interaction and condition monitoring framework using the digital twin system are investigated. With the designed framework, better synchronization of heating, uniform temperature, detection of hot spots, and stable heating performance can be achieved. However, its performance is degraded in the case of extremes, in which synchronization error reaches 2.8°C at maximum power and temperature uniformity error reaches 15.6°C at low ambient temperature. Moreover, the Transformer-BiLSTM model requires about (2.3×10^6) FLOPS per inference and 3.8 ms on RTX 4090. Such a requirement could make it challenging to deploy the proposed model on edge devices due to their limited computational resources. The geometrical adaptation out of the WK35 bucket (35 m^3, 20-80 mm wall thickness) is required through recalibration

Table 3. Ablation Experiment Performance Comparison

Experimental Configuration	Virtual-Physical Sync Error (°C)	Temperature Uniformity Std Dev (°C)	Power Response Delay (ms)	Anomaly Detection Accuracy (%)
Full system	1.2	8.5	42	98.5
Remove the multi-source perception fusion module	3.8	18.2	51	92.3
Remove the digital twin synchronization module	5.6	22.7	48	88.6
Remove the MQTT interactive control module	2.9	14.1	76	94.1
Remove Transformer-BiLSTM prediction module	1.5	10.3	46	86.9

of point cloud registration and meshing, but the thermal framework is not dependent on the geometry. In the case of 5% packet loss, synchronization error increases from 1.2°C to 1.8°C.

Competing of interests

The authors declare no competing of interests.

Authorship contribution statement

Jiayue Yu: Writing-Original draft preparation, Conceptualization, Supervision, Project administration.
Xing Zhao: Methodology
Xiaowen Song: Software
He Lv: Validation
Bin Yu: Formal analysis, Language review

Data availability

On Request

Declarations

Not applicable

Conflicts of interest

The authors declare that there is no conflict of interest regarding the publication of this paper.

Author statement

The manuscript has been read and approved by all the authors, the requirements for authorship, as stated earlier in this document, have been met, and each author believes that the manuscript represents honest work.

References

[1] X. Yang, Y. Li, Y. Yao, T. Qin, L. Yang, and Z. Sheng, (2025) *"Truck loading state estimation for autonomous operation of mining excavator"* **International Journal of Intelligent Robotics and Applications** ***9***(3): 1097–1108. DOI: https://doi.org/10.1007/s41315-024-00414-2.

[2] X. Wu, T. Yu, X. Liu, C. Yue, X. Jiang, J. Li, and Z. Li, (2026) *"Design of laser-assisted processing digital twin system"* **Journal of Manufacturing Systems** ***85***: 155–174. DOI: https://doi.org/10.1016/j.jmsy.2026.01.001.

[3] A. Love, S. Behseresht, O. A. V. Pastrana, J. Sakai, and Y. H. Park, (2025) *"Hybrid physical-virtual digital twin system for additive manufacturing"* **Journal of Advanced Manufacturing Systems** ***24***(01): 1–20. DOI: https://doi.org/10.1142/S0219686725500015.

[4] L. Yang and T. Özel, (2021) *"Physics-based simulation models for digital twin development in laser powder bed fusion"* **International Journal of Mechatronics and Manufacturing Systems** ***14***(2): 143–163. DOI: https://doi.org/10.1504/IJMMS.2021.119155.

[5] P. Stavropoulos, A. Papacharalampopoulos, V. Siatras, and D. Mourtzis, (2021) *"An AR based Digital Twin for Laser based manufacturing process monitoring"* **Procedia CIRP** ***102***: 258–263. DOI: https://doi.org/10.1016/j.procir.2021.09.044.

[6] Q. Li, Y. He, X. Geng, Y. Na, J. Su, X. Liu, B. Deng, Q. Zeng, and K. Zhang, (2026) *"Digital twin-driven condition monitoring methods for power electronic devices: Application and challenges"* **Renewable and Sustainable Energy Reviews** ***235***: 116983. DOI: https://doi.org/10.1016/j.rser.2026.116983.

[7] Z. Lei, H. Zhou, W. Hu, G.-P. Liu, S. Guan, and X. Feng, (2021) *"Toward a web-based digital twin thermal power plant"* **IEEE Transactions on Industrial Informatics** ***18***(3): 1716–1725. DOI: https://doi.org/10.1109/TII.2021.3086149.

[8] U. Tariq, R. Joy, S.-H. Wu, M. A. Mahmood, A. W. Malik, and F. Liou, (2023) *"A state-of-the-art digital factory integrating digital twin for laser additive and subtractive manufacturing processes"* **Rapid Prototyping Journal *29***(10): 2061–2097. DOI: https://doi.org/10.1108/RPJ-03-2023-0113.

[9] A. Feng, C. Chen, C. Wu, Y. Wei, and Y. Wang, (2022) *"Modeling of laser melting deposition equipment based on digital twin"* **Metals *12***(2): 169. DOI: https://doi.org/10.3390/met12020169.

[10] A. Gaikwad, R. Yavari, M. Montazeri, K. Cole, L. Bian, and P. Rao, (2020) *"Toward the digital twin of additive manufacturing: Integrating thermal simulations, sensing, and analytics to detect process faults"* **Iise Transactions *52***(11): 1204–1217. DOI: https://doi.org/10.1080/24725854.2019.1701753.

[11] A. Di Meglio, N. Massarotti, and P. Nithiarasu, (2024) *"A physics-driven and machine learning-based digital twinning approach to transient thermal systems"* **International Journal of Numerical Methods for Heat & Fluid Flow *34***(6): 2229–2256. DOI: https://doi.org/10.1108/HFF-10-2023-0616.

[12] A. Aminzadeh, S. Sattarpanah Karganroudi, M. S. Meiabadi, D. G. Mohan, and K. Ba, (2022) *"A survey of process monitoring using computer-aided inspection in laser-welded blanks of light metals based on the digital twins concept"* **Quantum Beam Science *6***(2): 19. DOI: https://doi.org/10.3390/qubs6020019.

[13] J. Chen, J. Clos, D. Price, and P. Caleb-Solly. "Digital twins for human-assistive robot teams in ambient assisted living". In: *Proceedings of the First International Symposium on Trustworthy Autonomous Systems*. 2023, 1–5. DOI: https://doi.org/10.1145/3597512.3597520.

[14] H. Qu, J. Chen, and Y. Cai, (2025) *"A digital twin approach for weld penetration prediction of tig welding with dual ellipsoid heat source"* **Journal of Intelligent Manufacturing *36***(6): 4083–4103. DOI: https://doi.org/10.1007/s10845-024-02431-1.

[15] F. Xiang, S. Zhou, Y. Zuo, and F. Tao, (2022) *"Digital twin driven end-face defect control method for hot-rolled coil with cloud-edge collaboration"* **IEEE Transactions on Industrial Informatics *19***(2): 1674–1682. DOI: https://doi.org/10.1109/TII.2022.3188508.

[16] Ł. Łach and D. Svyetlichnyy, (2026) *"Advanced numerical modeling of powder bed fusion: from physics-based simulations to AI-augmented digital twins"* **Materials *19***(2): 426. DOI: https://doi.org/10.3390/ma19020426.

[17] Z. Lin, C. Chen, Y. Zhang, J. Chen, Z. Liu, B. Qi, and J. Guo, (2026) *"An advanced IIoT gateway for enhanced data integration and real-time intelligence in digital twin manufacturing systems"* **Proceedings of the Institution of Mechanical Engineers, Part B: Journal of Engineering Manufacture *240***(4): 587–602. DOI: https://doi.org/10.1177/09544054251325968.

[18] Q. Lu, D. Zhu, M. Wang, and M. Li, (2023) *"Digital twin-driven thermal error prediction for CNC machine tool spindle"* **Lubricants *11***(5): 219. DOI: https://doi.org/10.3390/lubricants11050219.

[19] C. Liang, X. Li, W. Niu, and Y. Zhang, (2025) *"Internet of Things driven digital twin for intelligent manufacturing in shipbuilding workshops"* **Future Internet *17***(8): 368. DOI: https://doi.org/10.3390/fi17080368.

[20] S. Mihai, M. Yaqoob, D. V. Hung, W. Davis, P. Towakel, M. Raza, M. Karamanoglu, B. Barn, D. Shetve, R. V. Prasad, et al., (2022) *"Digital twins: A survey on enabling technologies, challenges, trends and future prospects"* **IEEE Communications Surveys & Tutorials *24***(4): 2255–2291. DOI: https://doi.org/10.1109/COMST.2022.3208773.

[21] J. Osho, A. Hyre, M. Pantelidakis, A. Ledford, G. Harris, J. Liu, and K. Mykoniatis, (2022) *"Four Rs Framework for the development of a digital twin: The implementation of Representation with a FDM manufacturing machine"* **Journal of Manufacturing Systems *63***: 370–380. DOI: https://doi.org/10.1016/j.jmsy.2022.04.014.

[22] T. Shen and B. Li, (2024) *"Digital twins in additive manufacturing: a state-of-the-art review"* **The International Journal of Advanced Manufacturing Technology *131***(1): 63–92. DOI: https://doi.org/10.1007/s00170-024-13092-y.

[23] V. Karkaria, Y.-K. Tsai, Y.-P. Chen, and W. Chen, (2025) *"An optimization-centric review on integrating artificial intelligence and digital twin technologies in manufacturing"* **Engineering Optimization *57***(1): 161–207. DOI: https://doi.org/10.1080/0305215X.2024.2434201.

[24] C. Zhang, J. Song, X. Yin, J. Cai, Y. Liang, and J. Lu, (2025) *"Digital twin-based approaches for agricultural machinery damage prediction and maintenance: A review"* **Journal of Computational Design and Engineering *12***(10): 87–117. DOI: https://doi.org/10.1093/jcde/qwaf097.

[25] A. J. Alvares, E. Rodriguez, and B. Figueroa, (2025) *"Digital-twin-enabled process monitoring for a robotic additive manufacturing cell using wire-based laser metal deposition"* **Processes *13***(8): 2335. DOI: https://doi.org/10.3390/pr13082335.

[26] Y. Li, S. Mojumder, Y. Lu, A. A. Amin, J. Guo, X. Xie, W. Chen, G. J. Wagner, J. Cao, and W. K. Liu, (2023) *"Statistical parameterized physics-based machine learning digital twin models for laser powder bed fusion process"* **arXiv preprint arXiv:2311.07821**: DOI: https://doi.org/10.48550/arXiv.2311.07821.

[27] L. Tudorache, Ö. Babur, S. S. Lucas, and M. van den Brand, (2025) *"Current approaches to digital twins in additive manufacturing: a systematic literature review"* **Progress in Additive Manufacturing *10***(12): 10819–10853. DOI: https://doi.org/10.1007/s40964-025-01262-7.

[28] B. Denkena, M. Wichmann, T. Malek, H. N. Nguyen, M. Kato, K. Isshiki, R. Koike, and Y. Kakinuma, (2024) *"Digital twin in process planning of the additive and subtractive process chain for laser metal deposition and micro milling of stainless steel"* **Journal of Manufacturing Science and Engineering *146***(7): 071004. DOI: https://doi.org/10.1115/1.4065415.

[29] M. J. Reynolds, E. R. Carter, D. T. Mitchell, and L. M. Brooks, (2026) *"Machine Learning-Based Prediction of Porosity Formation in Laser Powder Bed Fusion of Mechanical Components"* **Journal of Mechanical, Civil and Industrial Engineering *7***(3): 25–37.

[30] R. K. Phanden, S. Aditya, A. Sheokand, K. K. Goyal, P. Gahlot, and A. Jacso, (2022) *"A state-of-the-art review on implementation of digital twin in additive manufacturing to monitor and control parts quality"* **Materials Today: Proceedings *56***: 88–93. DOI: https://doi.org/10.1016/j.matpr.2021.12.217.

[31] C. Ma, H. Gui, and J. Liu, (2023) *"Self learning-empowered thermal error control method of precision machine tools based on digital twin"* **Journal of Intelligent Manufacturing *34***(2): 695–717. DOI: https://doi.org/10.1007/s10845-021-01821-z.

[32] A. W. Malik, M. A. Mahmood, and F. Liou, (2024) *"Digital twin–driven optimization of laser powder bed fusion processes: A focus on lack-of-fusion defects"* **Rapid Prototyping Journal *30***(10): 1977–1988. DOI: https://doi.org/10.1108/RPJ-02-2024-0091.

[33] S. K. Chokka, M. Nagaraju, and K. Nagabushan Kumar, (2024) *"Digital twin in welding"* **Automation in Welding Industry: Incorporating Artificial Intelligence, Machine Learning and Other Technologies**: 91–109. DOI: https://doi.org/10.1002/9781394172948.ch6.

[34] S. P. Murzin, (2024) *"Artificial intelligence-driven innovations in laser processing of metallic materials"* **Metals *14***(12): 1458. DOI: https://doi.org/10.3390/met14121458.

[35] S. Liu, Y. Sun, P. Zheng, Y. Lu, and J. Bao, (2022) *"Establishing a reliable mechanism model of the digital twin machining system: An adaptive evaluation network approach"* **Journal of Manufacturing Systems *62***: 390–401. DOI: https://doi.org/10.1016/j.jmsy.2021.12.008.

[36] X. Zhang, L. Zhou, G. Feng, K. Xi, H. Algadi, and M. Dong, (2025) *"Laser technologies in manufacturing functional materials and applications of machine learning-assisted design and fabrication"* **Advanced Composites and Hybrid Materials *8***(1): 76. DOI: https://doi.org/10.1007/s42114-024-01154-4.